

CORROSION BEHAVIOR OF SiMo DUCTILE CAST IRON IN DIFFERENT CORROSIVE ENVIRONMENTS

Dawlat M. Abdelrahim  and Ebtesam E. Ateia

Physics Department, Faculty of Science, Cairo University, Giza, Egypt

Adel A. Nofal

Department of Foundry Technology, Central Metallurgical Research and Development Institute (CMRDI), Helwan 11421, Cairo, Egypt

Mona H. Gomaa and Z. Abdel Hamid

Corrosion Control and Surface Protection Department, Metal Technology Institute, Central Metallurgical R&D Institute (CMRDI), P.O. Box 87, Helwan, Cairo 11421, Egypt

Copyright © 2023 The Author(s)
<https://doi.org/10.1007/s40962-023-01112-8>

Abstract

Standard SiMo ductile cast iron automotive alloys are typically subjected to various hostile environmental conditions. For the current investigation, SiMo with a silicon content of 5% and molybdenum contents ranging from 0 to 1.5% was used. In two corrosive environments of 0.6 M NaCl and 0.5 M H₂SO₄, the study intends to present the corrosion behavior of high silicon molybdenum ductile cast iron (SiMo). Moreover, the impact of changing Mo on the microstructural characteristics has been investigated. The SEM-EDX examinations revealed that the nodule counts, M₆C carbides, and lamellar pearlite increased while the ferritic matrix decreased with increasing Mo contents. It is clear that the addition of Mo reduces cast iron's rate of corrosion and thus increases its corrosion resistance. The

results showed that SiMo cast iron alloy with 1.0 wt% Mo had a lower corrosion current (I_{corr}) in 0.6 M NaCl solution while lower corrosion current (I_{corr}) with the cast iron containing 1.5 wt% Mo in 0.5 M H₂SO₄ solution, which resulted in the lowest corrosion rate. The occurrence of a galvanic couple between the alloy matrix and the graphite nodules results in electrochemical corrosion, with the largest corrosion rates taking place at Mo-free alloy in both media.

Keywords: SiMo, molybdenum contents, exhaust gas, electrochemical corrosion

Introduction

Numerous automotive components are still produced using castings due to the benefits of design flexibility and weight savings that cast complements can offer. Ferritic SiMo ductile cast iron has a silicon content of 3.5–5% and a molybdenum content of 0.4–1.5% (wt%).^{1,2} It is frequently used for high-temperature applications due to its favorable thermomechanical properties, including high-temperature tensile strength and resistance to creep rupture because of the formation of a matrix of complex Fe–Mo

carbides at the grain boundaries³ as well as beneficial combinations of static strength and ductility for the reason of the high silicon contents.⁴

More stringent emissions regulations that call for cleaner, more efficient engines must be complied with by the automotive industry. An additional objective is to boost engine performance while preserving low fuel consumption. The specifications for high-temperature corrosion and the mechanical operation of engine parts are getting stricter. This is especially applicable for the turbocharger housing and exhaust manifold of the exhaust system.⁵

The temperature of the exhaust gases from large diesel engines is frequently not far from 700 °C.⁶ The manifold temperature cycles that occur during start–stop engine operation cause a thermal gradient. In addition, the components that would lower the exhaust gas temperature in heavy-duty trucks are a liquid-cooled system (using engine coolant) and an air-cooled system.⁷ Exhaust gases basically consist of nitrogen, water vapor, oxygen, and carbon oxides. Smaller concentrations of HC compounds, nitrogen oxides, and sulfur oxides are also present. These oxides produce nitric and sulfuric acid droplets when they interact with water vapor. Low exhaust gas temperatures cause water vapor to condense in the exhaust manifold pipes with other vapors of sulfuric acid H₂SO₄ and nitric acid HNO₃.⁸ The entire surface of exhaust channels is severely corroded by such chemically aggressive nitric or sulfuric acid condensates, which also support extensive in-depth corrosion.⁹ At about 56 °C, all sulfuric acid has almost completely condensed.¹⁰

Due to the free graphite content of cast iron (3–4% by weight or 10% by volume), corrosion of cast iron leaves behind an insoluble graphitic layer of corrosion products. These corrosion products are extremely strong, adherent, and dense, and they create a barrier that prevents further corrosion.¹¹ Because cast iron can be protected from corrosive processes by the graphite layer, the presence of microcells does not have a very significant impact on the rate of corrosion for cast iron. The high casting tightness,¹² particularly the absence of slag inclusions and gas porosity,¹³ thermal–mechanical conditions,¹⁴ environmental elements, double film inclusions,¹⁵ and decarburization process¹⁶ all have a positive impact on corrosion resistance. Nofal et al.¹⁷ stated that ductile iron exhibited better corrosion resistance than the gray iron in the NaCl solution at its different concentrations. This is because ductile iron has the tendency of forming a uniformly distributed graphite phase as well as forming a barrier film.

Nearly all published works focus on the SiMo ductile iron's oxidation behavior at high temperatures above 700 °C. However, there are no studies on the SiMo corrosion that might happen as a result of exhaust gas condensation on the exhaust manifold channels during cooling

cycles. Moreover, the corrosion behavior of SiMo in aqueous solution is poorly understood. Components made of SiMo DI are similarly susceptible to corrosion caused by the outside environment, such as rain and chloride solution. Therefore, understanding how SiMo DI corrodes in aqueous environments as a function of Mo contents is crucial and could help with material loss analysis.

This research looked at how the Mo content affected the corrosion resistance of SiMo cast iron. Electrochemical methods were used to study the corrosion behavior in 0.6 M NaCl and 0.5 M H₂SO₄ solutions at ambient temperature.

Experimental Procedure

Material

The melting of SiMo alloys with various Mo contents took place in a medium-frequency induction furnace with a 100 kg capacity. High-purity (Sorel) pig iron, steel scrap, ferrosilicon (75%), ferromolybdenum (60%), and carburizing material made up the base molten iron. The molten metal was treated at 1520°C with a 1.4% Mg–Fe–Si spheroidizing alloy containing 9–10% Mg, while the inoculant (70–76% Si, 0.75–1.25% Ca, 0.75–1.25% Al, 1.5–2% Zr, and Fe [Bal.]) with particle size (0.7–3 mm) was added.

The sandwich technique was used for the inoculation and spheroidization treatments. In this technique, the Fe–Si–Mg alloy was put in a pocket that was built into the ladle bottom and covered with high-grade low-carbon steel turnings. As a result of the physical barrier was formed between the Fe–Si–Mg alloy and the liquid iron, slowing the reaction time, increasing alloy use efficiency (magnesium recovery), and reducing flame and flaring. Afterward, the molten alloys were poured into a cylindrical greensand mold of dimensions of 35 mm diameter and a height of 220 mm. The chemical composition of the SiMo ductile iron samples is listed in Table 1.

Table 1. The Chemical Composition of SiMo Iron Samples

Sample	Chemical composition, wt%									
	C	Si	Mo	Mn	P	Cu	S	Cr	Mg	Fe
S1	3.27	5.08	0.02	0.21	0.014	0.128	0.0017	0.043	0.021	Bal.
S2	3.26	5.11	0.54	0.19	0.013	0.125	0.0016	0.044	0.032	Bal.
S3	3.25	5.17	1.06	0.20	0.011	0.13	0.0020	0.041	0.031	Bal.
S4	3.20	5.22	1.53	0.22	0.013	0.126	0.0021	0.045	0.028	Bal.

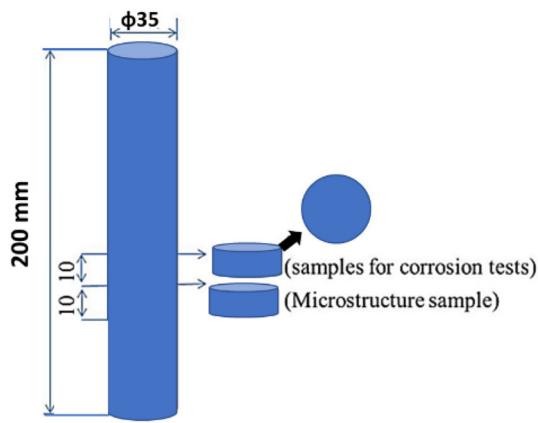


Figure 1. Position of samples for microstructure investigation and corrosion tests.

Metallographic Investigation

Samples (10 mm thick) were cut at a height of 80 cm from the rod bottom. Figure 1 depicts the placement of the specimens used for microstructure and corrosion examinations. The samples were machined as disks of 25 mm in diameter and 10 mm in thickness. To perform a metallographic investigation to look at the microstructure, the samples were polished and etched in 2% Nital for 5 minutes at room temperature then well washed with water and dried. The nodule count and nodularity were calculated in unetched samples at a 100x magnification using the ZEISS image analyzer software according to ISO 945-1 and ISO 945-4. Grenier et al.¹⁸ provided a full description and analysis of the nodule count and nodularity measurements method utilizing image analysis. Field emission scanning electron microscopy (FE-SEM; Quanta EG) outfitted with energy-dispersive X-ray spectroscopy (EDX) was used to analyze the microstructure, eutectic carbides, and fine precipitate phases forming close to the cell boundaries of SiMo cast iron samples.

Corrosion Test

To assess the corrosion performance of the various samples, electrochemical impedance spectroscopy (EIS) and potentiodynamic polarization measurements were made with 0.5 M H₂SO₄ acidic solution and 0.6 M NaCl solution at ambient temperature. Before the corrosion test, samples were mechanically polished using SiC sheets of varying grits, washed in water, and dried.

Utilizing the IviumStat instrument, electrochemical measurements were made (supplied by Ivium Technologies, Eindhoven, the Netherlands). IviumStat instrument can be managed by a computer using the IviumSoft software (the Netherlands) (PC), as illustrated in Figure 2. The personal computer (PC) was used to specify the measurement's parameters, display the measured curves, and compute the

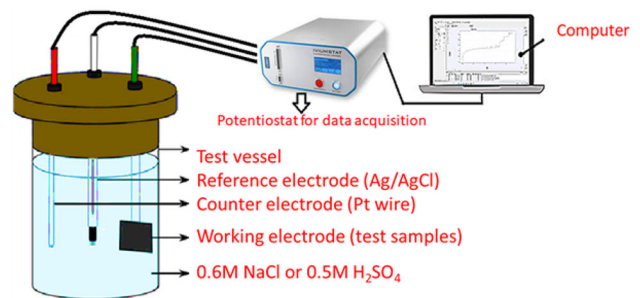


Figure 2. A schematic drawing of IviumStat instrument displays the main parts.

measurement's outcomes. The software enables automatic or manual calculation of the I_{corr} and Tafel slopes depending on the Tafel line's shape. The Tafel lines were recorded using the potentiodynamic polarization technique, which automatically changed the electrode potential from -500 mV (cathodic direction) to $+500$ mV (anodic direction) at a scan rate of 0.5 mVs^{-1} . To achieve this, a three-electrode system was used, with a platinum sheet serving as the counter electrode, a working electrode with a surface area of 0.785 cm^2 , and a silver/silver chloride electrode (Ag/AgCl) serving as the reference electrode, which has an E° of 199 mV vs. normal hydrogen electrode (NHE). The open-circuit potential (OCP) was maintained steady for 30 min while the three electrodes were submerged in 0.6 M NaCl solution or $0.5 \text{ M H}_2\text{SO}_4$ acid solution. The intersection of the anodic and cathodic lines at zero polarization was named the corrosion current (I_{corr}). Using alternating current (AC) signals with an amplitude value of 10 mV and a frequency range of $35 \text{ kHz} - 100 \text{ mHz}$, the impedance of the coated samples was tested. The equivalent circuit based on the OCP was used to analyze the results of the impedance test.

Results and Discussion

Microstructure Investigation

The changes in the high Si DI microstructure owing to the variation in Mo content are shown in the OM microstructures (Figure 3). The 0% Mo sample has a fully ferritic matrix and a significant amount of nodular graphite (Figure 3a). On the other hand, the microstructures of SiMo ductile iron alloys with different Mo contents are similar. The three SiMo alloys are made up of nodular graphite and different amounts of fine precipitates that are dispersed throughout the ferrite matrix (Figure 3b–d). The nodule count and the percentage of ferrite, pearlite, and graphite, as well as cell-boundary precipitated carbides in each alloy, were calculated using Zeiss microscopy software for metallographic analysis, as listed in Table 2. The highest nodule count was at 0% Mo, while the nodular count gradually decreased with increasing Mo contents. The volume fraction of cell-boundary precipitates increased significantly with the increased Mo contents while ferrite

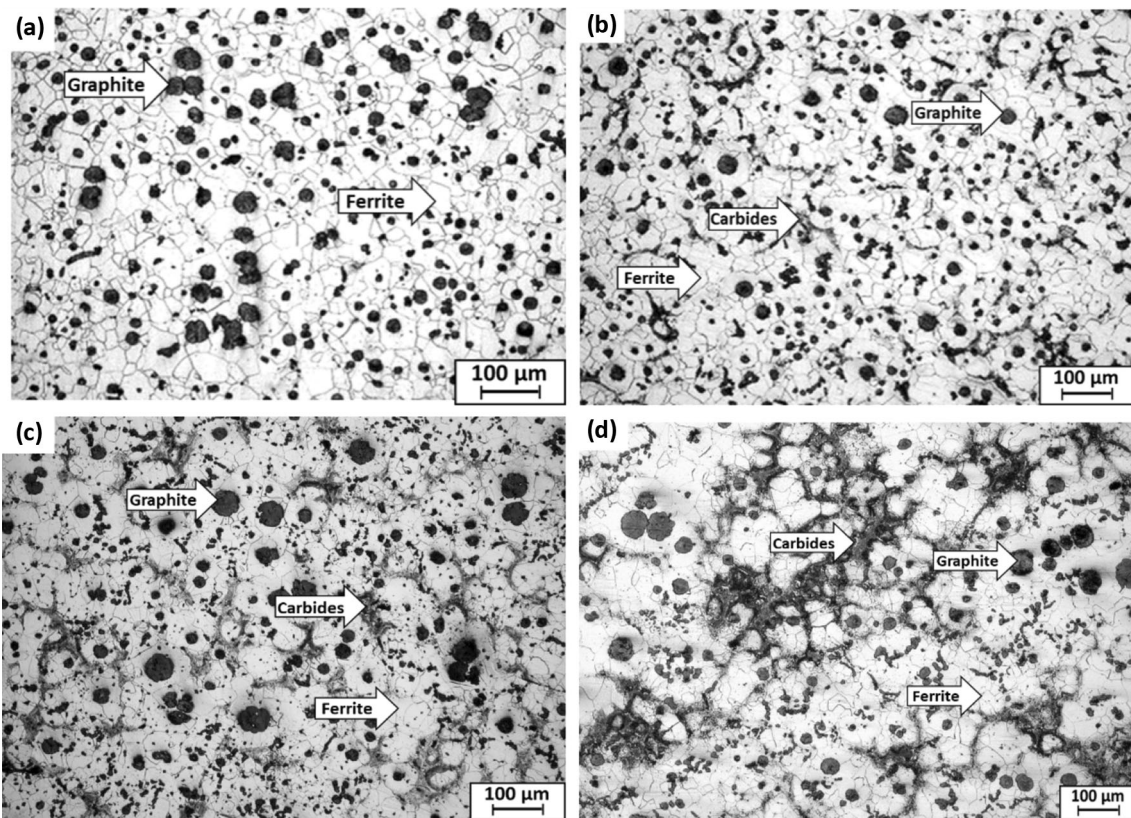


Figure 3. Microstructure of SiMo ductile iron: (a) 0% Mo, (b) 0.5% Mo, (c) 1% Mo, and (d) 1.5% Mo. Nital (2%) etched samples (100x magnification).

Table 2. Microstructure Calculations of Examined SiMo Samples

Sample	Nodule count (Nod/mm ²)	Nodularity (%)	Graphite (%)	Ferrite, (%)	Pearlite, (%)	Carbide, (%)
S1	455	75.33	13.30	86.65	–	0.05
S2	402	72.14	11.67	76.88	10.41	1.04
S3	339	64.31	11.13	70.61	16.06	2.2
S4	223	59.74	10.68	65.53	19.79	4

decreased (Table 2). This is due to the high tendency of molybdenum to segregate at cell boundaries.^{19,20}

For further investigation by SEM, these precipitates were in the matrix of SiMo ductile iron. Fishbone-similar precipitates are present at grain boundaries, and both lamellar pearlite and finely spherical carbides surround these fishbone-similar precipitates (Figure 4). From EDS analysis (see Figure 5), these fishbone-similar precipitates are proposed to be M_6C carbides ($M = Mo, Si, \text{ and } Fe$), containing almost 32% of Mo. The amount of M_6C carbides and the surrounding fine precipitates of lamellar pearlite increases with increasing Mo contents; consequently, the percentage of ferrite decreases. These obtained results agree well with earlier microstructural investigations mentioned in the previous works.^{19–22}

The total number of graphite nodules reduces as the Mo content increases, but its size and distribution are only slightly affected, according to Figures 6 and 7. Table 2 also shows that an increase in Mo contents led to a decrease in nodularity almost from 75 to 60%. This might be the case because factors such as section thickness, inoculation effectiveness, and pouring temperature have an impact on the graphite's size and distribution. As shown in Figure 6, the inoculant with $Zr+O+S$ in the current study encourages the formation of graphite nodules with a variety of sizes and distributions. Due to Zr's affinity for oxygen and sulfur, which results in heterogeneous oxides and sulfides, graphite can form at these locations.²³

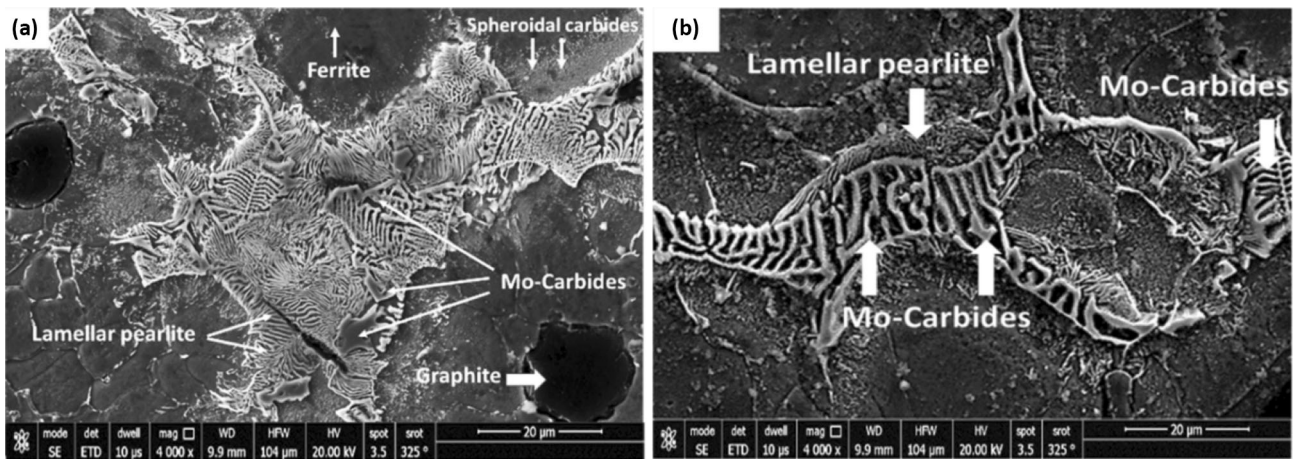


Figure 4. SEM photomicrographs of SiMo ductile iron exhibit: (a) grain-boundary precipitates and (b) fishbone-similar carbides at 1% Mo sample.

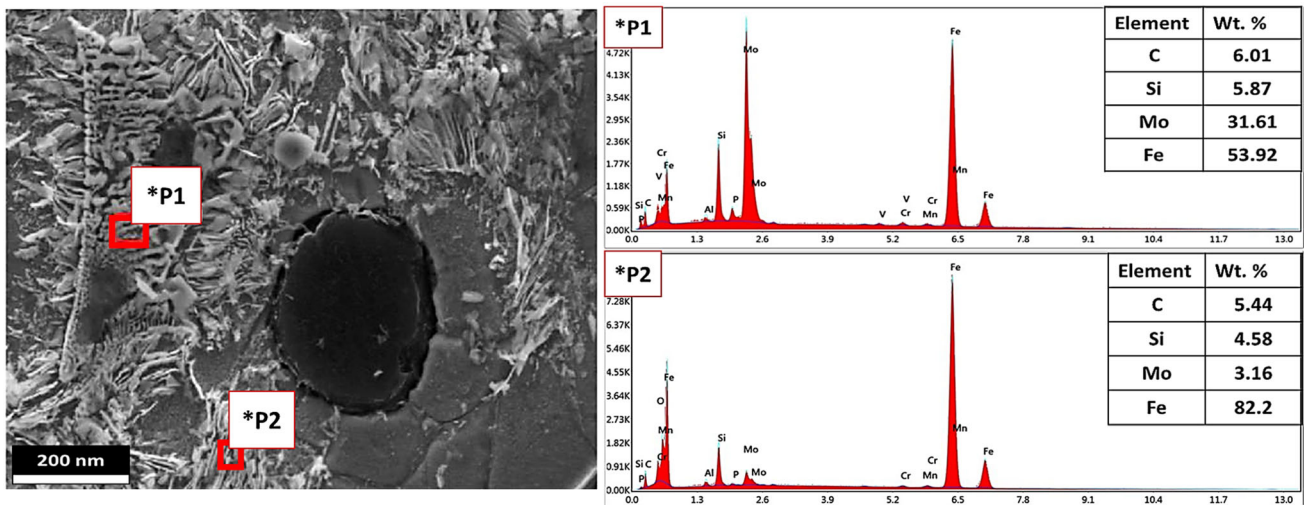


Figure 5. SEM-EDX analysis for Mo-rich carbides of SiMo ductile iron (0.5% Mo).

Corrosion Measurement

To evaluate the corrosion resistance of SiMo cast iron with various Mo contents in different environments, electrochemical techniques (electrochemical polarization and electrochemical impedance) were used.

Electrochemical polarization measurement

Electrochemical polarization measurement was used to gauge each sample's corrosion resistance. The measurement was carried out in 0.6 M NaCl and 0.5 M H₂SO₄ solutions at ambient temperature as shown in Figure 8a–b. The figure shows the cathodic and anodic polarization curves for SiMo cast iron containing various Mo contents in 0.6 M NaCl and 0.5 M H₂SO₄ solutions. Using polarization curves as a starting point, the Tafel extrapolation method is used to calculate the corrosion potential (E_{corr}), corrosion current density (I_{corr}), and polarization resistance

(R_p) using polarization curves. Table 3 provides a summary of the findings.

For the corrosion evaluation in NaCl solution, first, the open-circuit potential of the SiMo samples was measured as a function of time at 25°C in 0.6 M NaCl aerated solution until the steady-state value is reached, and then, the polarization measurements using Tafel lines were carried out and presented in Figure 8a and Table 3. The results revealed that a lower corrosion current density value ($2.895 \times 10^{-5} \text{ A/cm}^2$) was recorded for the sample containing 1 wt% Mo than the other cast iron investigated samples, and consequently, a lower corrosion rate (0.2186 mm/y) was obtained compared with the corrosion rate of cast iron 0 wt% Mo (1.415 mm/y) (Table 3). This may be attributed to reduce the formation of nodular graphite which led to reduce the galvanic effects.

A ferrite metallic matrix, graphite nodules, and the amount of segregation in the form of carbides (i.e., Fe₂MoC and

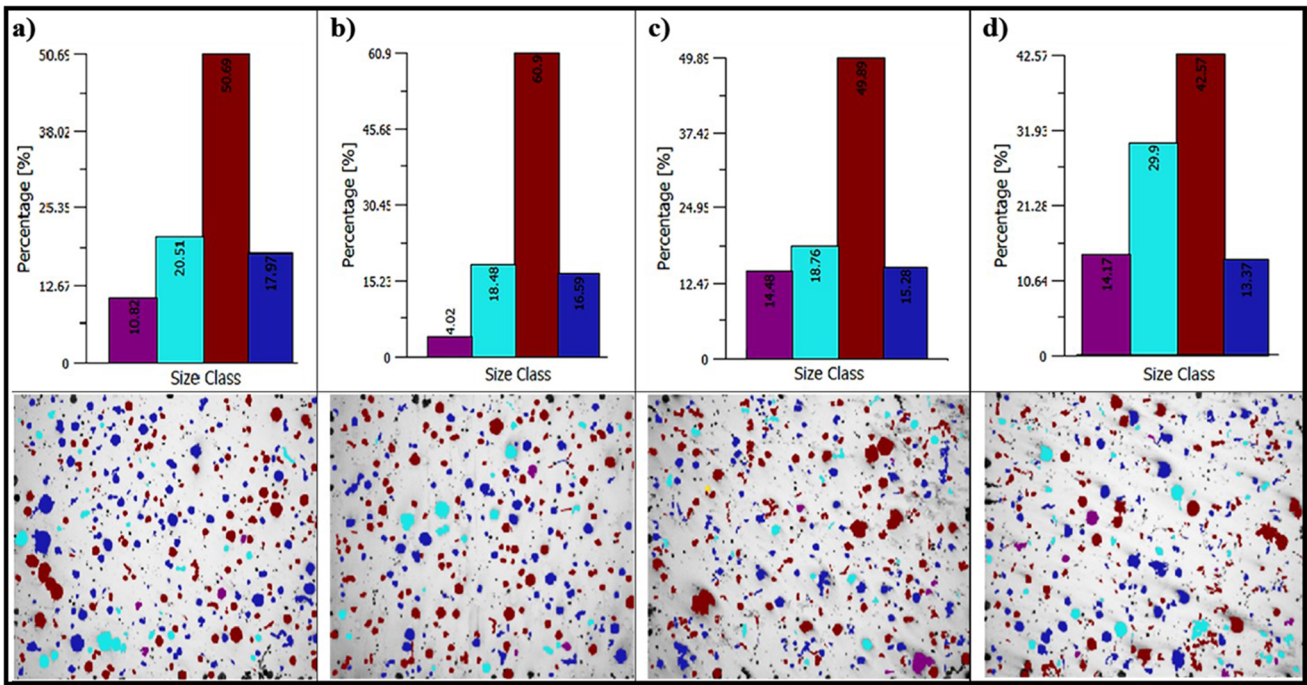


Figure 6. Size distribution of the nodular graphite in all SiMo alloys: (a) 0% Mo, (b) 0.5% Mo, (c) 1% Mo, and (d) 1.5% Mo, attached by result images at 100x magnifications.

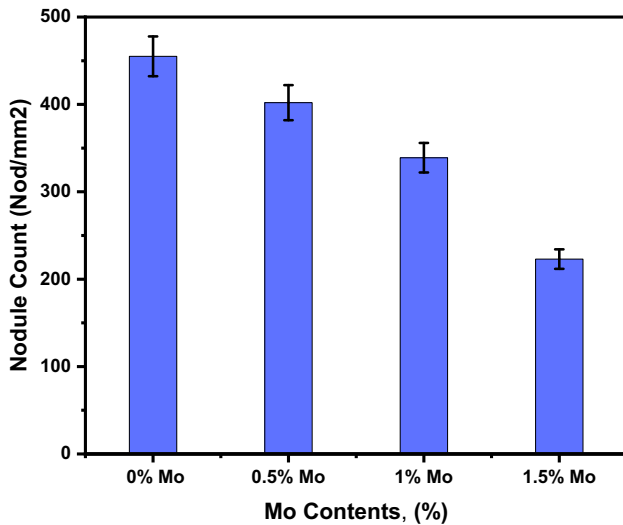


Figure 7. Nodule count vs. Mo contents.

M₆C) surrounded by a pearlite island make up the majority of the SiMo ductile iron's microstructure (Figure 4) and each phase having its own electrochemical potential. These disparities in potential could result in the accumulation of leftover cementite and graphite at the cathodic sites and the dissolution of the less noble ferrite matrix phase at the anodic site. These multiphases in the microstructure have a significant impact on the corrosion resistance. Since graphite has a higher electrochemical potential than the ferrite matrix, micro-galvanic cells are created at the graphite-matrix interface. Galvanic coupling causes the matrix surrounding the graphite to dissolve preferentially, leaving

cavities and a porous mass of corrosion products in the area of the graphite nodule. Graphitic corrosion is a term used to describe this phenomenon.²⁴

The pH of a solution has an important factor in determining the corrosion resistance of materials because hydrogen ions can interact and change the surface and therefore alter the corrosion resistance of a material. Figure 8b and Table 3 illustrate the effect of 0.5 M H₂SO₄ solutions on the corrosion behavior of SiMo containing different Mo contents. For the corrosion evaluation in H₂SO₄, the results indicate that all the sample alloys have suffered from corrosion to varying extents during the polarization test in this solution, with a much higher corrosion rate than in a 0.6 M NaCl solution.

When SiMo alloy reacts with an aggressive solution (0.5 M H₂SO₄), which causes a quick interaction between acid and air, a soluble passive layer (oxide film) forms on the surface of cast iron. It results in no protection being provided on the surface and prevents a solution from emerging. Iron corrosion in H₂SO₄ solution generally demonstrated that hydrogen depolarization occurs. The anodic dissolution reaction (Eqn. 1) and the analogous cathodic reaction (Eqn. 2) can be used to describe the spontaneous dissolving of iron. According to Mathur and Vasudevan,²⁵ the hydrogen evolution reaction, which takes place in two phases (Eqns. 3 and 4), is cathodically responsible for controlling the corrosion of metals in acidic solutions.



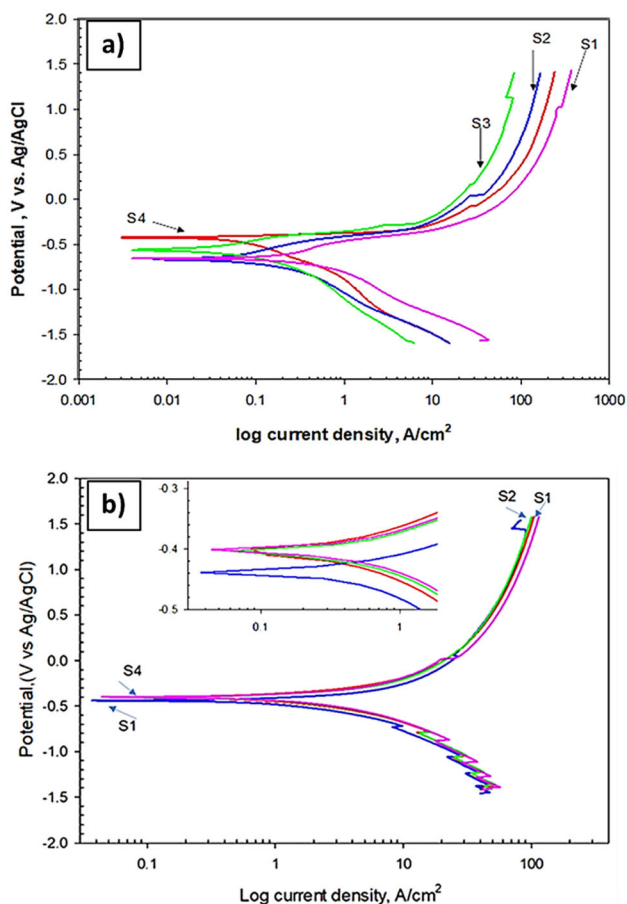
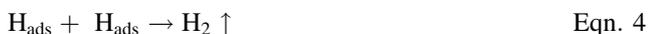


Figure 8. Anodic and cathodic potentiodynamic polarization curves at different corrosive mediums: (a) 0.6 M NaCl and (b) 0.5 M H₂SO₄.

Table 3. The Polarization Parameters of Different SiMo Cast Irons in 0.5 M H₂SO₄ and 0.6 M NaCl Solution

Medium	Sample	E_{corr} V	I_{corr} A/cm ²	R_p	Corrosion rate, mm/y
NaCl	0% Mo	-0.637	18.70	274.9	1.415
	0.5% Mo	-0.665	5.80	896.3	0.440
	1% Mo	-0.556	2.89	1491.0	0.2186
	1.5% Mo	-0.451	8.79	318.2	0.656
H ₂ SO ₂	0% Mo	-0.414	119.5	47.8	9.02
	0.5% Mo	-0.435	94.0	42.2	7.09
	1% Mo	-0.400	88.4	42.7	6.67
	1.5% Mo	-0.394	79.0	43.8	5.96



The E_{corr} of the SiMo containing various Mo contents was

approximately unaltered in the H₂SO₄ solutions. In contrast, the I_{corr} markedly dropped as Mo was raised up to 1.5 wt% Mo. The results showed that SiMo cast iron alloy with 1.5 wt% Mo had a lower corrosion current (I_{corr}) (79.0×10^{-5} A/cm²) in the H₂SO₄ solution, which resulted in the lowest corrosion rate (5.958 mm/y) compared with the free Mo cast iron (Table 3).

According to this study, as the molybdenum level rose, the amount of nodular graphite decreased, its size somewhat increased, the amount of ferrite dropped, and the graphite/matrix contact weakened. These elements reduce corrosion rate, improving corrosion resistance. Contrarily, as the number of Mo-rich precipitates (such as carbides and lamellar pearlite) increases, the rate of corrosion increases and the corrosion resistance decreases in the samples. As a result, the improvement in corrosion resistance was mitigated by this aspect. In order to prevent the development of unintended carbides that affect corrosion behavior, the Mo content must be kept within a certain range.

A transition layer of corrosion reaction products is created on the surface of the exhaust piping as a result of the reaction between the exhaust gas condensates and the material. The intensity of oxygen penetration into the wall depth is influenced by the diffusion of oxygen into the metal and, conversely, the diffusion of reaction products toward the surface, as well as by the elemental potential of cast iron and the compactness of the corroded layer. After the corrosion test, the corrosion on the sample's surface is comparatively uniform. To better understand the corrosion behavior of SiMo alloys in such a corrosive condition, optical microscopy was used to examine the corroded surface of sample materials. Figure 9 depicts the corroded surfaces along with their microstructure. From the inspection of the surfaces after the corrosion test, it can be seen that the nodular graphite sites are what the corrosive medium targets the most. As shown in Figure 9, the ferrite matrix for the 0% Mo sample erodes more slowly than the nodular graphite, which is also partially degraded. Figure 9 shows that in SiMo samples, the ferritic matrix is less degraded than the nodular graphite that is followed by Mo precipitates. In comparison with the NaCl medium, the corroded surfaces in the sulfuric acid medium appeared to be significantly more corroded. This is due to the quicker corrosion rate as was previously mentioned.

According to earlier research, corrosion resistance is enhanced by reducing the amount of nodular graphite present.^{26,27} At the ferrite grain boundary, the high impurity concentration and potential may lead to boundary instability. Additionally, the creation of an electrochemical circuit is facilitated by the potential difference between graphite and ferrite.²⁸ Moreover, corrosion resistance is related to the graphite/matrix interface. Although the current study found that higher Mo levels (more than 1.5 wt%) decrease nodular graphite and ferrite, their positive

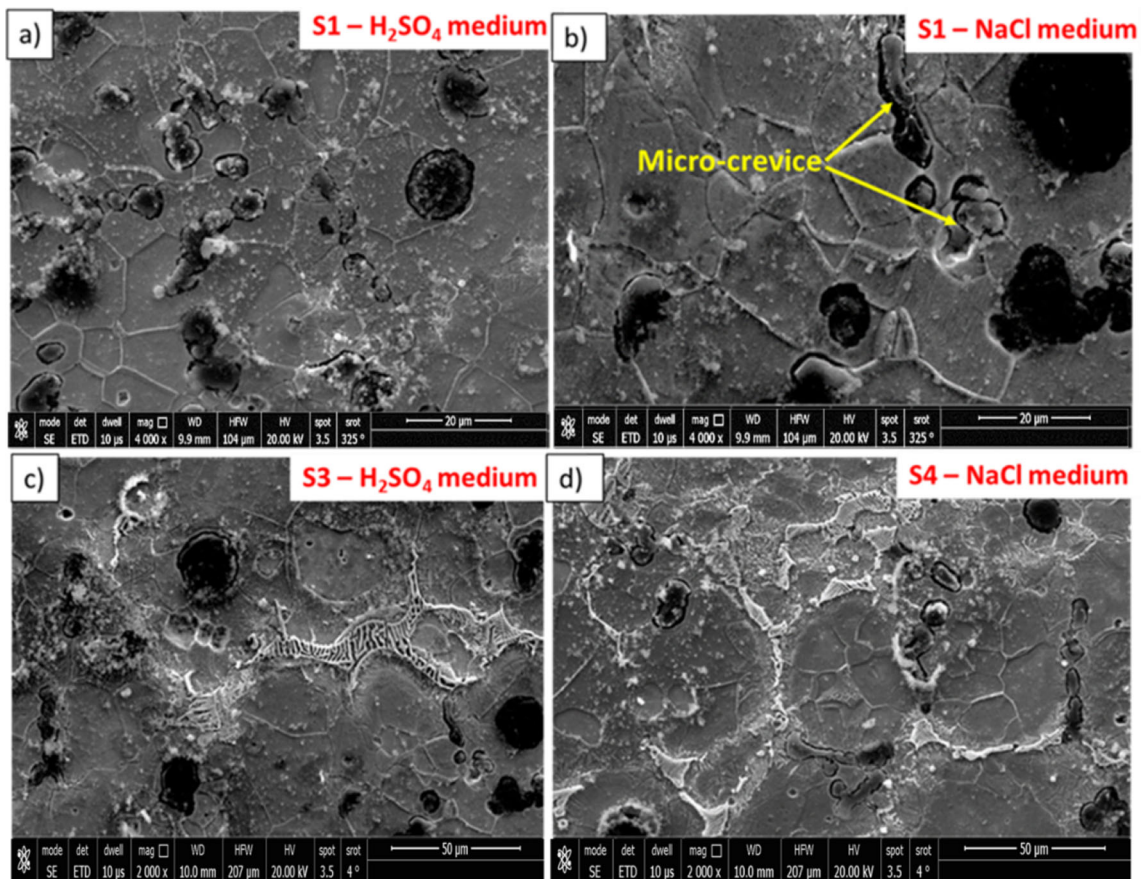


Figure 9. The corroded surfaces of some investigated samples.

influence on corrosion resistance was not surprising. This means that the amount of nodular graphite and the number of Mo precipitates present in the microstructure both affect the corrosion behavior of SiMo ductile iron.

Electrochemical impedance spectroscopy (EIS)

Electrochemical impedance spectroscopy was used to examine the corrosion behavior of SiMo cast iron containing different Mo contents in 0.6 M NaCl and 0.5 M H₂SO₄ solutions. The electrochemical impedance diagrams are depicted in Figure 10a–b and Table 4. The impedance spectra were given in the Nyquist representation. All the impedance data points were analyzed using the equivalent circuit shown in Figure 10 (inset figure). This equivalent circuit fitted well with the experimental results. The main parameters deduced from the analysis of the Nyquist diagram are the solution resistance R_s , the charge transfer R_{ct} (diameter of the high-frequency loop), Warburg diffusion (W), and the capacitance of double-layer C_{dl} .

In Figure 9a, for the evaluation of corrosion behavior in 0.6 M NaCl solution, it is clear that the Nyquist plots of the different samples of cast iron show a depressed semicircular shape. The inset image in Figure 10a depicts the circuit model of the

examined samples that were used to further match the EIS test parameters and assess the corrosion behavior. This model matched the outcomes of the experiment. Voltage is applied across the circuit as a result of the Warburg diffusion one-time constant. The impedance spectra for the corrosion product generated by the corrosion process on the surface after exposure to a corrosive electrolyte (0.6 M NaCl) are explained using this model. This observation indicates that the corrosion of cast iron in 0.6 M NaCl solution is mainly controlled by a charge transfer process and that the corrosion process is characterized by a single time constant with Warburg diffusion $R_s (R_{ct}C_{dl}W)$, implying the presence of a double layer at the sample surface/electrolyte interface.²⁹ The high charge transfer resistance value ($R_{ct}=197.7 \Omega$) for the currently examined sample S3 compared to free Mo cast iron sample S1 (164 Ω) implies that Mo has a good effect on corrosion resistance up to 1.0 wt%.

The Nyquist plots are not perfect semicircles and are generally attributed to the frequency dispersion and mass transport resistance. C_{dl} stands for double-layer capacitance, which is basically the capacitance between the electrolyte and the working electrode. In order to account for the deflection of the frequency dispersion semicircle caused by an experimental system due to surface inhomogeneity, surface roughness, electrode porosity, surface

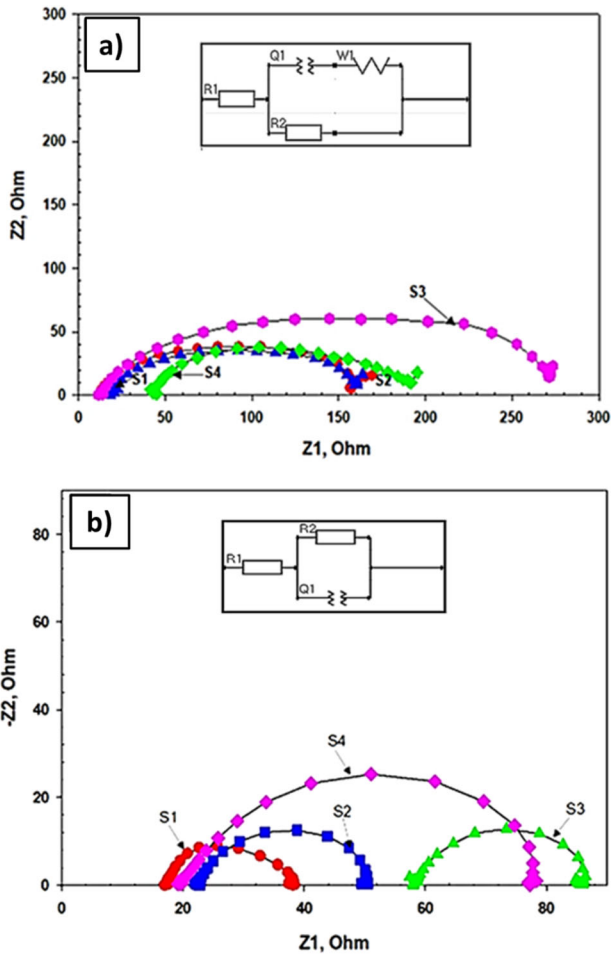


Figure 10. The Nyquist plots of impedance spectra for SiMo cast iron in 0.6 M NaCl and H₂SO₄ solutions.

Table 4. EIS Parameters of the Investigated Samples in NaCl and H₂SO₄ Solutions

Medium	Sample	R_s, Ω	R_{ct}, Ω	$W, \times 10^2$	$CPE, \times 10^{-2}$	n	Chi-square
NaCl	0% Mo	6.39	168.5	7.77	4.62	1.0	1.1
	0.5% Mo	12.9	164.0	3.39	1.65	1.0	0.82
	1% Mo	11.7	197.7	4.47	0.068	1.0	1.0
	1.5% Mo	36.8	164.0	6.26	0.855	1.0	1.0
H ₂ SO ₄	0% Mo	17.9	19.5	–	0.0108	1.0	0.17
	0.5% Mo	22.8	26.0	–	0.0191	1.0	0.32
	1% Mo	58.3	26.76	–	0.0205	1.0	0.29
	1.5% Mo	21.17	54.3	–	0.0104	1.0	0.49

disorder, geometric irregularities, and others, a constant phase element (CPE) must be used in place of a pure capacitor, as is done in the case of pure capacitors.³⁰

The main parameters deduced from the Nyquist diagram are reported in Table 4. These parameters illustrated that the value of R_{ct} increases with increasing the Mo contents and the maximum value with 1.0 wt% Mo, while the value of double-layer capacitance C_{dl} (CPE) decreases. This attributed to the increase in thickness of the electric double layer, suggested that Mo gives better protection against corrosion. These results are in good agreement with the results obtained from the potentiodynamic polarization electrochemical technique.

The inset image in Figure 10b represents the circuit model of the samples under scrutiny that was used to further match the EIS test parameters and assess the corrosion behavior. This model was used to describe the impedance spectra for the corrosion product formed by the corrosion process on the surface exposed to a corrosive electrolyte (0.5 M H₂SO₄) and matched the experimental data. The circuit is, therefore, a one-time constant. The main parameters deduced from the analysis of the Nyquist diagram which is reported in Table 3 illustrated that the value of R_{ct} increases with increasing the Mo contents and the maximum value (54.3 Ω) with 1.5 wt% Mo, while the value of double-layer capacitance C_{dl} (CPE) decreases. These findings are well in line with those of the electrochemical potentiodynamic polarization technique.

Conclusions

The variation in Mo content affects the microstructure of SiMo cast iron and hence the corrosion behavior as well. The corrosion behavior of SiMo ductile cast iron has been investigated through potentiodynamic polarization measurements and EIS in 0.6 M NaCl and 0.5 M H₂SO₄ solutions. The results of this investigation suggest some conclusions, which can be summarized as follows:

1. The microstructure of Mo-free DI contains a significant amount of nodular graphite in a fully ferritic matrix, while SiMo alloys consist of nodular graphite, M₆C carbides, and lamellar pearlite, embedded in a ferritic matrix due to Mo segregation at grain boundaries according to SEM-EDX investigations.
2. The results revealed that the microstructure plays a chief role in the corrosion behavior as the extent of corrosion was related to the Mo content.
3. The SiMo containing 1 wt% Mo has lower corrosion rates in 0.6 M NaCl solution, while the SiMo containing 1.5 wt% Mo has lower corrosion rates in 0.5 M H₂SO₄ solution.
4. The analysis of potentiodynamic polarization and microstructure results showed that the corrosion of SiMo ductile cast iron may be due to the galvanic action resulting from the difference in

electrode potential between the nodular graphite and the matrix in all studied samples.

Funding

Open access funding provided by The Science, Technology & Innovation Funding Authority (STDF) in cooperation with The Egyptian Knowledge Bank (EKB).

Open Access

This article is licensed under a Creative Commons Attribution 4.0 International License, which permits use, sharing, adaptation, distribution and reproduction in any medium or format, as long as you give appropriate credit to the original author(s) and the source, provide a link to the Creative Commons licence, and indicate if changes were made. The images or other third party material in this article are included in the article's Creative Commons licence, unless indicated otherwise in a credit line to the material. If material is not included in the article's Creative Commons licence and your intended use is not permitted by statutory regulation or exceeds the permitted use, you will need to obtain permission directly from the copyright holder. To view a copy of this licence, visit <http://creativecommons.org/licenses/by/4.0/>.

REFERENCES

1. M. Ekström Oxidation and corrosion fatigue aspects of cast exhaust manifolds (PhD dissertation, KTH Royal Institute of Technology). (2015). Retrieved from <http://urn.kb.se/resolve?urn=urn:nbn:se:kth:diva-166274>
2. S.N. Lekakh, V.A. Athavale, L. Bartlett et al., Effect of micro-structural dispersity of SiMo ductile Iron on thermal cycling performance. *Inter Metalcast* (2022). <https://doi.org/10.1007/s40962-022-00915-5>
3. S.N. Lekakh, C. Johnson, L. Godlewski et al., Control of high-temperature static and transient thermomechanical behavior of SiMo ductile Iron by Al alloying. *Inter Metalcast* **17**, 22–38 (2023). <https://doi.org/10.1007/s40962-022-00768-y>
4. D. Franzen, B. Pustal, A. Bührig-Polaczek, Influence of graphite-phase parameters on the mechanical properties of high-silicon ductile Iron. *Inter Metalcast* **17**, 4–21 (2023). <https://doi.org/10.1007/s40962-022-00761-5>
5. M. Ekström, Development of a ferritic ductile cast iron for improved life in exhaust applications (Licentiate dissertation, KTH Royal Institute of Technology) (2013). Retrieved from <http://urn.kb.se/resolve?urn=urn:nbn:se:kth:diva-122006>.
6. S. Mao, Z. Feng, E.E. Michaelides, Off-highway heavy-duty truck under-hood thermal analysis. *Appl. Therm. Eng.* **30**(13), 1726–1733 (2010). <https://doi.org/10.1016/j.applthermaleng.2010.04.002>
7. B.J. Yang, S. Mao, O. Altin, Z.G. Feng, E.E. Michaelides, Condensation analysis of exhaust gas recirculation system for heavy-duty trucks. (2011). <https://doi.org/10.1115/1.4004745>
8. F. Tholence, M. Norell, High temperature corrosion of cast alloys in exhaust environments I-Ductile cast Irons. *Oxid Met* **69**, 13–36 (2008). <https://doi.org/10.1007/s11085-007-9081-y>
9. J. Roučka, E. Abramová, V. Kaňa, Properties of type SiMo ductile irons at high temperatures. *Archives of Metallurgy and Materials*, 63 (2018)
10. MP. Perujo, Condensation of water vapor and acid mixtures from exhaust gases (Doctoral dissertation, Verlag nicht ermittelbar), (2004).
11. T. Fredric, High temperature corrosion of cast Irons and steels chalmers university of technology (2004).
12. M.P. Brady, G. Muralidharan, D.N. Leonard et al., Long-term oxidation of candidate cast Iron and stainless steel exhaust system alloys from 650 to 800 °C in air with water vapor. *Oxid Met* **82**, 359–381 (2014). <https://doi.org/10.1007/s11085-014-9496-1>
13. M. Stawarz, P.M. Nuckowski, Effect of Mo addition on the chemical corrosion process of SiMo cast Iron. *Materials*. **13**(7), 1745 (2020). <https://doi.org/10.3390/ma13071745>
14. M.M. Ibrahim, A. Nofal, M.M. Mourad, Microstructure and hot oxidation resistance of SiMo ductile cast Irons containing Si-Mo-Al. *Metall Mater Trans B* **48**, 1149–1157 (2017). <https://doi.org/10.1007/s11663-016-0871-y>
15. G. Gyarmati, G. Fegyverneki, M. Tokár, T. Mende, Investigation on double oxide film initiated pore formation in Aluminum casting alloys. *Int J Eng Manag Sci* **5**(2), 141–153 (2021)
16. S.N. Lekakh, M. Buchely, R. O'Malley, L. Godlewski, M. Li, Thermo-cycling fatigue of SiMo ductile iron using a modified thermo-mechanical test. *Int. J. Fatigue* **148**, 106218 (2021)
17. A. Nofal, A.S.I. Ahmed, W.A. Ghanem, W.A. Hussein, N.K. Mohamed, Evaluation of corrosion behavior of different grades of cast Iron insodium chloride solutions. *Key Eng. Mater.* **835**, 223–228 (2020). <https://doi.org/10.4028/www.scientific.net/kem.835.223>
18. S. Grenier, C. Labrecque, A. Bhattacharjee et al., Inter-laboratory study of nodularity and nodule count of ductile Iron by image analysis. *Inter Metalcast* **8**, 51–63 (2014). <https://doi.org/10.1007/BF03355582>
19. D.M. Abdelrahim, E.E. Ateia, A.A. Nofal, Effect of molybdenum contents on microstructure and high-temperature wear behavior of SiMo ductile Iron. *Inter Metalcast* (2023). <https://doi.org/10.1007/s40962-023-01012-x>

20. KH. Choe, KW. Lee, MH. Kim, Effect of Mo on the microstructure and thermal expansion of high Si ferritic heat-resistant ductile iron. In 2015 International Conference on Materials, Environ Biol Eng (pp. 967-972). Atlantis Press. (2015)
21. M. Youssef, A. Nofal, A. Hussein, Influence of Cooling Rate on Nature and Morphology of Intercellular Precipitates in Si-Mo Ductile Irons. In Materials Science Forum (Vol. 925, pp. 231–238). Trans Tech Publications, Ltd. (2018). <https://doi.org/10.4028/www.scientific.net/msf.925.231>
22. L. Dekker, B. Tonn, Occurrence and behaviour of Mo containing precipitates in nodular cast iron at high temperatures. *Int. J. Cast Met. Res.* **29**(1–2), 85–91 (2016). <https://doi.org/10.1179/1743133615Y.0000000024>
23. L. Riposan and T. Sakaland, In *Cast Iron Science and Technology*, (ed) Stefanescu D M, ASM International, 1A (2017).
24. G. Palumbo, M. Górný, A. Bitka, Influence of the cooling rate on mechanical and corrosion properties of ferritic Si–Mo ductile cast Iron. *Metall Mater Trans A* **54**, 2362–2373 (2023). <https://doi.org/10.1007/s11661-023-07023-x>
25. P.B. Mathur, T. Vasudevan, Reaction rate studies for the corrosion of metals in acids—I, iron in mineral acids. *Corrosion* **38**(3), 171–178 (1982)
26. S. Gollapudi, Grain size distribution effects on the corrosion behaviour of materials. *Corros. Sci.* **62**, 90–94 (2012). <https://doi.org/10.1016/j.corsci.2012.04.040>
27. C.H. Hsu, M.L. Chen, Corrosion behavior of nickel alloyed and austempered ductile irons in 3.5% sodium chloride. *Corros Sci* **52**(9), 2945–2949 (2010). <https://doi.org/10.1016/j.corsci.2010.05.006>
28. H. Krawiec, J. Lelito, E. Tyrąła et al., Relationships between microstructure and pitting corrosion of ADI in sodium chloride solution. *J Solid State Electrochem* **13**, 935–942 (2009). <https://doi.org/10.1007/s10008-008-0636-x>
29. G. Instruments, Basics of electrochemical impedance spectroscopy. G. Instruments, Complex impedance in Corrosion, 1-30 (2007).
30. Z. Abdel Hamid, Mona H. Gomaa, Soliman I. El-Hout, Emad M.M. Ewais, “ α -Fe₂O₃/Fe₃O₄@GO nanosheets boost the functionality of Ni–P thin film deposited by electroless method”, *Surface & Coatings Technology* 456 (2023) 129288. <https://doi.org/10.1016/j.surfcoat.2023.129288>

Publisher’s Note Springer Nature remains neutral with regard to jurisdictional claims in published maps and institutional affiliations.